



Contents lists available at ScienceDirect

International Journal of Mechanical Sciences

journal homepage: www.elsevier.com/locate/ijmecsci

Temperature-regulated surface charge manipulates ionic current rectification in tapered nanofluidic channel

Amer Alizadeh^{a,c}, Wei-Lun Hsu^a, Hirofumi Daiguji^{a,*}, Moran Wang^{b,*}

^a Department of Mechanical Engineering, The University of Tokyo, Tokyo 113-8656, Japan

^b Department of Engineering Mechanics, Tsinghua University, Beijing 100084, China

^c Department of Chemical and Petroleum Engineering, Schulich School of Engineering, University of Calgary, Calgary, AB T2N 1N4 Canada

ARTICLE INFO

Keywords:

Nanofluidic diode
Temperature dependent surface charge
Ionic current rectification
Electrical double layer
Lattice Boltzmann method

ABSTRACT

Diverse ionic current rectification methods for nanofluidic chips have recently emerged. Herein, we theoretically demonstrate that by applying a temperature gradient to the aqueous solution, the ionic rectification property of a tapered nanochannel can be manipulated by applying temperature gradients from the tip to base and vice versa. Our modeling results reveal that the rectification ratio can be significantly enhanced by applying a temperature increment from the base to tip, whereas the rectification ratio is significantly suppressed by applying a reverse temperature gradient. In addition to the solution temperature, we also investigated the influence of bulk ionic strength and tip height on the rectification ratio, thereby providing overlapping and non-overlapping regimes of electrical double layers. We demonstrate that the rectification behavior of a tapered nanochannel is determined by the overlapping regime of the electrical double layer at the tip of the nanochannel. Moreover, we propose a semi-analytical solution that can capture numerical results with the same order of magnitude. We expect that the modeling results of this contribution can provide a direction for understanding ionic transport across geometrically and thermally asymmetrical media, which could find applications from energy conversion to logical nanofluidic chip components.

1. Introduction

Ion transport through nanometer-sized channels or porous membranes has attracted interest owing to the unexpected phenomena that have been observed on this small scale [1]. The governing of ion transport by surface charge [2], assisting biological modification for manipulating electrical conductance [3], electrostatically controlling ion transport [4–7], energy conversion [8–11], water treatment [12], DNA translocation through nanoslits [13] and thermal manipulation of the electrical conductance [14,15] are examples of the promising and breakthrough applications of this new field of science and technology. Among these nanofluidic applications, imitating the ion transport functionality of ionic channels in biological membranes is the source of nanofluidic diodes, which resembles the function of electrical diodes [16]. The first typical design of nanofluidic diodes was based on a conical nanochannel that mimicked an ionic channel and provided an asymmetric distribution of ions, resulting in a nonzero variation of the electrical double layer (EDL) thickness along the nanochannel [16–20]. Siwy et al. [21] found that the ionic strength and pH of a solution

significantly influenced the rectifying ratio (ratio of forward to reverse bias current). They experimentally demonstrated that by decreasing the ion concentration to 0.1 mM, the rectification ratio of the conical nanochannel was enhanced to four. The ion rectification effect can be achieved by introducing asymmetric reservoir concentrations into a homogeneous straight nanochannel. Clearly, the ion concentration in one reservoir should be sufficiently low to overlap the EDL [22]. The overlapping of the EDLs alongside the nanochannel walls results in asymmetric electrostatic effects, where the overlapped region will be counter-ion-selective. Cheng and Guo [22] demonstrated that by increasing the nanochannel height ($H = 20\text{nm}$), the rectification ratio of the nanochannel increased to 3.5 when the right and left reservoirs were subjected to bulk ion concentrations $c_R = 0.1\text{M}$ and $c_L = 10^{-4}\text{M}$, respectively. To obtain stronger ion rectification effects, Daiguji et al. [6] theoretically and later Karnik et al. [23] experimentally demonstrated a nanofluidic diode that acquired positive–negative and positive–neutral surface charges, respectively. Following the idea of inhomogeneous material design, different methods have been proposed, such as modifying the surface chemistry of conical PET membranes [24]

* Corresponding authors.

E-mail addresses: daiguji@thml.t.u-tokyo.ac.jp (H. Daiguji), mrrwang@tsinghua.edu.cn (M. Wang).

<https://doi.org/10.1016/j.ijmecsci.2021.106754>

Received 20 April 2021; Received in revised form 14 July 2021; Accepted 17 August 2021

Available online 19 August 2021

0020-7403/© 2021 Elsevier Ltd. All rights reserved.

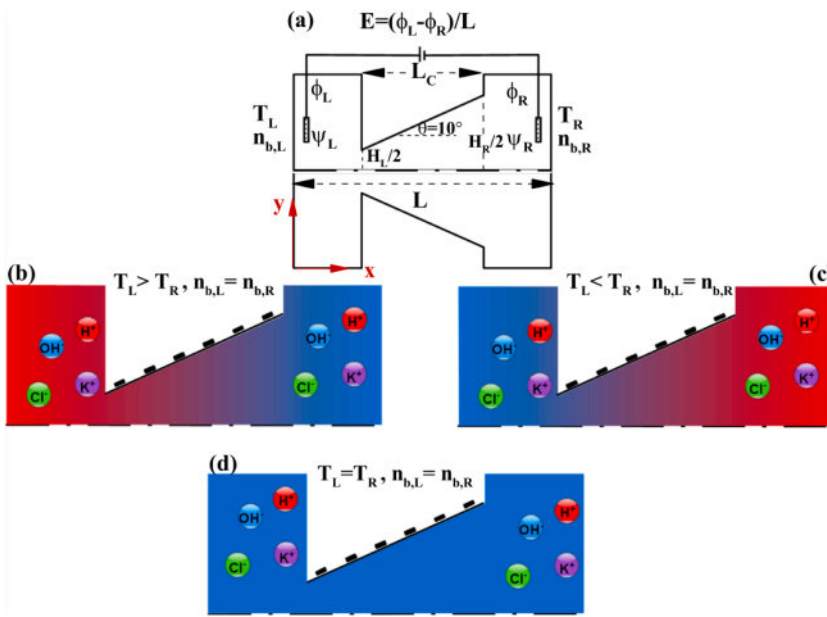


Fig. 1. (a) Schematic depiction of tapered homogeneous nanochannel with applied electric field for forward bias as $\phi_L > \phi_R$, and reverse bias $\phi_L < \phi_R$. The two reservoirs have the same concentrations of ions $n_{b,L} = n_{b,R}$ and assume that the walls are electrically charged because of the chemical reaction with bulk solution ($\psi_{L,w} = \zeta(n_{b,L}, T_L)$, $\psi_{R,w} = \zeta(n_{b,R}, T_R)$). The zeta potential on the nanochannel walls is a function of the local temperature and ion concentration $\zeta = f(T(x), c_{K^+}(x))$. (b) Tapered nanochannel under nonzero temperature gradient $T_L > T_R$, which decreases from left to right. (c) Increasing from left to right $T_L < T_R$. (d) Zero temperature gradient $T_L = T_R$. The blue and red colors represent the low (30 °C) and high solution temperatures (50 °C), respectively.

and utilizing different solid oxide materials with different isoelectric points [25,26]. Very recently, a novel design of nanofluidic diode was presented by Li and Li [27] that controlled the nanochannel size and surface charge by layer-by-layer deposition of charged polyelectrolytes on the PDMS channel walls. This novel method of nanofluidic diode with heterogeneous wall's materials demonstrated a significant impact on the rectifying ionic current. The main bottleneck for this nanofluidic diode type is the manufacturing process of inhomogeneous materials along the nanochannel. To address this challenge, researchers have attempted to impose surface charge inhomogeneity along the nanochannels by utilizing highly asymmetric pH values for both reservoirs [28–31] or solute concentration gradients as mentioned above. Another important parameter that not only manipulates the ion distribution [14,32] but also the acquired surface charge on the solid–aqueous interfaces [14, 33–36] is the temperature of the solution. Venditti et al. [33] experimentally demonstrated that the zeta potential of a microchannel is a function of the solution temperature. They demonstrated that the sensitivity of the zeta potential to the variation of the solution temperature at the glass– or polydimethylsiloxane–aqueous interface decreases by decreasing the bulk ion strength. The temperature effects on the acquired surface charge have been recognized as the main reason for the temperature-dependent measured ionic currents and nanochannel conductance [14,37–39]. Imposing a temperature gradient on the micro/nanochannel interfaces [40] and the uniform electrically gated nanochannel [38,41] has demonstrated that the ion selectivity could be enhanced because of the variation in solution viscosity and, consequently, the ionic diffusivity (Stokes–Einstein relation). Exploiting the temperature-dependent surface charge could be an interesting idea to study the influence of the temperature gradient on the ionic rectification phenomenon in such a homogeneously fabricated conical nanochannel. Despite the numerous ionic rectification methods in nanofluidic channels that have been discussed, to the best of the authors' knowledge, no work has been reported on the temperature gradient effects on the ionic rectification phenomenon in nanofluidic devices related to the temperature effects on the surface charge.

In this work, we employ a temperature-dependent electrical quadrupole (EQL) model [39] based on a recently proposed EQL model [42] to obtain the surface charge and zeta potential at the silica–aqueous interface as a function of the local solution properties such as temperature, ion concentration, and pH. Successively, by solving the temperature-dependent EQL model (see Supporting information)

coupled with the Poisson–Nernst–Planck and Navier–Stokes equations, we theoretically study the temperature-regulated ion rectification phenomenon in tapered nanochannels. To this objective, two temperature gradients ($\nabla T > 0$ and $\nabla T < 0$) as well as an isothermal temperature field ($\nabla T = 0$) are applied to the nanochannel under forward and reverse bias electrical fields and two bulk ionic strengths ($n_b = 0.1$ mM and $n_b = 1$ mM) to investigate the selectivity of the tapered nanochannel. The two bulk ionic strengths allow the study of the influence of different temperature-regulated surface charge sensitivities [33]. The coupled Poisson–Nernst–Planck and Navier–Stokes equations are solved using coupled lattice Boltzmann models. Finally, we propose a simple semi-analytical solution to discuss the ion selectivity of the nanofluidic channels.

2. Problem definition

Fig. 1 displays the schematic of a tapered nanochannel ($\theta = 10^\circ$) with $H_L = 10$ nm, $H_R = 80.53$ nm, $L_C = 0.2\mu\text{m}$, and $L = 0.52\mu\text{m}$ designed for the present study (Fig. 1(a)). The reservoir heights are assumed to be $H = 17H_L$, which provides sufficiently large reservoirs compared to the nanochannel tip for our numerical study. In this setup, we assume that the ion concentration and pH of the solution at both reservoirs are equal. According to the above discussion, the temperature can manipulate the acquired surface charge and consequently, the zeta potential [33,39] of the silica–aqueous interface. Venditti et al. [33] experimentally demonstrated that the sensitivity of the zeta potential to the temperature is directly related to the bulk ion concentration. Thus, applying a temperature gradient accompanied by a different bulk ionic strength can provide interesting ion rectification effects. This temperature-regulated ion rectification must be investigated in the presence of an applied external electric field. Fig. 1(b) and (c) indicate that we considered two temperature gradients, where $\nabla T < 0$ and $\nabla T > 0$; Fig. 1(d) displays the isothermal scenario $\nabla T = 0$.

In this contribution, we assume that (i) the two reservoirs, which include the solution and walls, are sufficiently large to be considered as thermal energy reservoirs and (ii) the nanochannel's wall temperature linearly changes from left to right. These assumptions guarantee the provision of a cross-sectionally constant and steady-state temperature at the inlet and outlet of the nanochannel. Conversely, ignoring the convection heat transfer because of the extremely low Reynolds ($Re \approx 0.01$, see Supporting information) fluid flow allows using the average cross-

section temperature of the nanochannel, which justifies the linear distribution of the temperature along the nanochannel as $T(x) = T_L + \frac{(T_R - T_L)x}{L}$ (see Supporting information). To obtain the local ion concentration, we solve the modified Nernst–Planck equations [32]

$$\frac{\partial c_i}{\partial t} + \mathbf{u} \cdot \nabla c_i = D_i \nabla^2 c_i + z_i D_i \left(\nabla \cdot (c_i \nabla (\bar{\psi} + \bar{\phi})) \right) - \frac{c_i}{T} \nabla T \cdot \nabla (\bar{\psi} + \bar{\phi}) \quad (1)$$

For each ionic species, where c_i , D_i , and z_i denote the i^{th} ion concentration, diffusion, and valance number, respectively. $\bar{\psi} = \frac{\psi}{V_T}$ and $\bar{\phi} = \frac{\phi}{V_T}$ are the dimensionless electric potential and applied electric potential ($E = -\nabla\phi$), respectively, where $V_T = \frac{k_B T}{e}$ is the thermal voltage, $k_B = 1.38 \times 10^{-23} \text{ JK}^{-1}$ is the Boltzmann constant, and $e = 1.602 \times 10^{-19} \text{ C}$ is the basic charge of an electron. Considering the right-hand side of Eq. (1), the last term represents the thermo-electrochemical migration phenomenon [32] which provides the influence of thermal and electrical gradients on the ionic transport through an applied temperature gradient. Clearly, this term is dropped for an isothermal scenario, whereby Eq. (1) is reduced to the conventional format of the modified Nernst–Planck equation. However, in the presence of a temperature gradient and zero potential difference on the electrodes ($\nabla\phi = 0$), the temperature gradient as an external source induces an internal electric field ($\nabla\psi$) owing to the temperature effects on the surface charge of the nanochannel walls. This effect is different from the well-known thermo-diffusion phenomenon, which is identified as the Soret effect [43] and is negligible for even the lowest applied electric fields [41]. Thus, in this study, we ignore the Soret effect in our modeling results. Moreover, we do not consider the influence of temperature on the ionic diffusivity because it has been demonstrated that temperature-dependent diffusivity does not significantly change the ionic rectification ratio [41]. This assumption allows us to solely elucidate the influence of the temperature-regulated surface charge on the rectification ratio of the tapered nanofluidic channel.

In Eq. (1), we decompose the electric field into the internal electric potential (ψ) due to the influence of EDL on the distribution of the ionic species and external electric field (E). In this study, the nanochannel walls acquire a local electric charge because of the chemical reaction with the bulk aqueous solution, which is considerably less than the applied external electric field. Conversely, we assume that the nanochannel walls are insulated to the applied external electric field and that the nanochannel walls can only be electrically charge through the zeta potential. This inconsistency in the boundary conditions for the two electric fields imposes formidable difficulty in solving the Poisson equation [38,41,44]. Consequently, the electric field can be decomposed to obtain the internal electric field by solving the Poisson equation as [28]

$$\nabla^2 \psi = -\frac{\rho_e}{\epsilon_0 \epsilon_r}, \quad (2)$$

where ρ_e , $\epsilon_0 = 8.854 \times 10^{-12} \text{ CV}^{-1} \text{ m}^{-1}$, and $\epsilon_r = 305.7 \exp\left(-\frac{T_{\text{inc}}}{219}\right)$ [45]

are the free net electric charge density ($\rho_e = \sum_i z_i e c_i$), vacuum electrical permittivity, and ratio of water permittivity to vacuum for an average temperature ($T_{\text{ave}} = (T_L + T_R)/2$), respectively. To solve Eq. (1), it is subjected to zero ionic flux boundary conditions ($j_i = 0$) at the walls and Dirichlet-type boundary conditions at the inlet ($c_{i,L} = n_{b,L}$) and outlet ($c_{i,R} = n_{b,R}$). For Eq. (2), we assume that the nanochannel walls acquire surface charge exclusively owing to local thermo-chemical properties ($\zeta(x)$, $\sigma_0(x) \neq 0$), whereas the reservoirs acquire a homogeneous surface charge solely because of the reservoir solution temperature and bulk ionic strength.

To obtain the zeta potential as a boundary condition for Eq. (2), we employ a temperature-dependent surface-complexation model [39]. In this model, after introducing temperature-dependent parameters such as

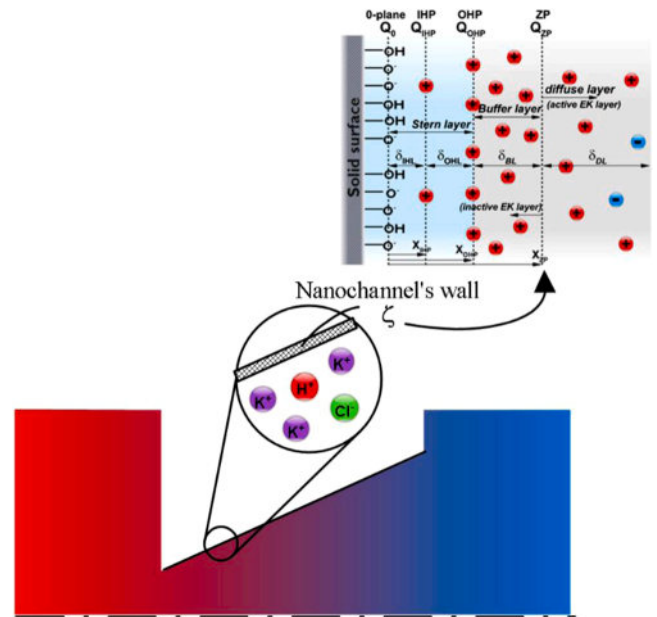
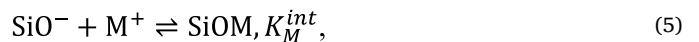
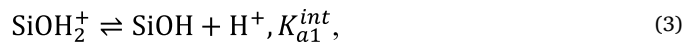


Fig. 2. Schematic illustration of employing EQL model [39] to obtain zeta potential on nanochannel walls.

solution electrical permittivity and chemical equilibrium constants into the surface complexation model, the surface charge and zeta potential are obtained based on the local thermochemical properties of the solution. Hence, the typical chemical reactions on the silica surface are considered as [39]



where M^+ denotes the local concentration of the cation, and K_{a1}^{int} , K_{a2}^{int} , and K_M^{int} are the inert chemical equilibrium constants. In this model, the local effective bulk ion concentration is obtained based on the local solution properties [46]. Once the thermochemical properties of the solution are obtained, the local zeta potential and surface charge can be obtained. Fig. 2 illustrates the employment of the temperature-dependent EQL model for our nanochannel walls. This model considers three series capacitances near the silica surface, which represent the layers of the EDL where a flexible buffer layer is added to the Stern and diffuse layers. Adding the buffer layer facilitates determining the position of the zeta potential plane as a function of the solution concentration and temperature.

The applied external electric field generates an electroosmotic flow through the nanochannel. To obtain the flow field, we solve the modified incompressible Navier–Stokes equations

$$\begin{aligned} (a) : & \nabla \cdot \mathbf{u} = 0, \\ (b) : & \frac{\partial(\mathbf{u})}{\partial t} + \mathbf{u} \cdot \nabla(\mathbf{u}) = -\frac{1}{\rho} \nabla p + \nabla \cdot [v \nabla(\mathbf{u})] + \frac{\mathbf{F}}{\rho}, \end{aligned} \quad (6)$$

where $\rho(\text{kgm}^{-3})$ is the density of the electrolyte, $\mathbf{u}(\text{ms}^{-1})$ is the flow velocity, $p(\text{Pa})$ is the fluid pressure, $v(\text{m}^2\text{s}^{-1})$ is the kinematic viscosity, and $\mathbf{F} = -\rho_e(\nabla\phi + \nabla\psi)$ is the electrical body force density with a dimension of Nm^{-3} . Note that we did not apply a pressure gradient to drive the solution. Therefore, the fluid flow is triggered only by applying an external electric field. To solve the governing equations Eqs. (1), (2) and (6), we employ the lattice Boltzmann method, which is discussed in detail elsewhere [28,32,47–49]. Here we must point out that we wrote a

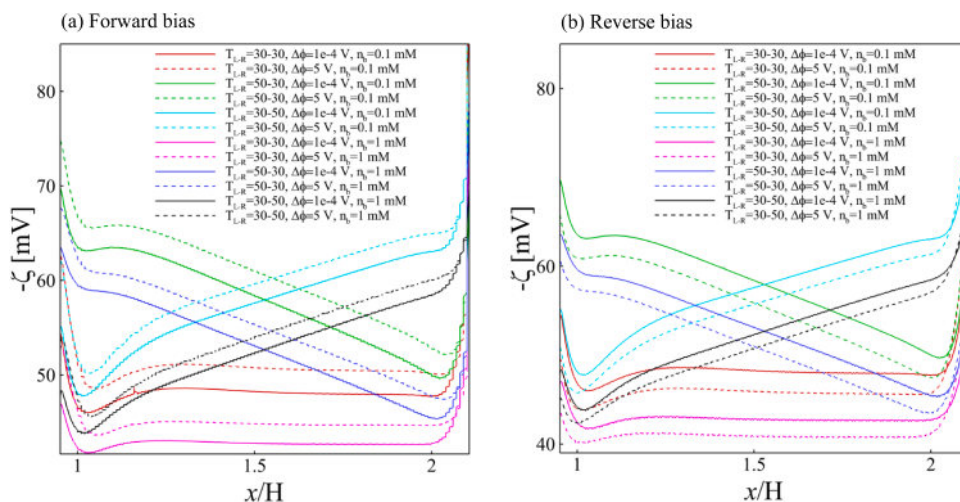


Fig. 3. Zeta potential as function of tapered nanochannel length for (a) forward and (b) reverse bias electric fields. The solid lines represent the low applied voltage ($|\Delta\phi| = 10^{-4} \text{V}$) and the dashed lines the high voltage ($|\Delta\phi| = 5 \text{V}$).

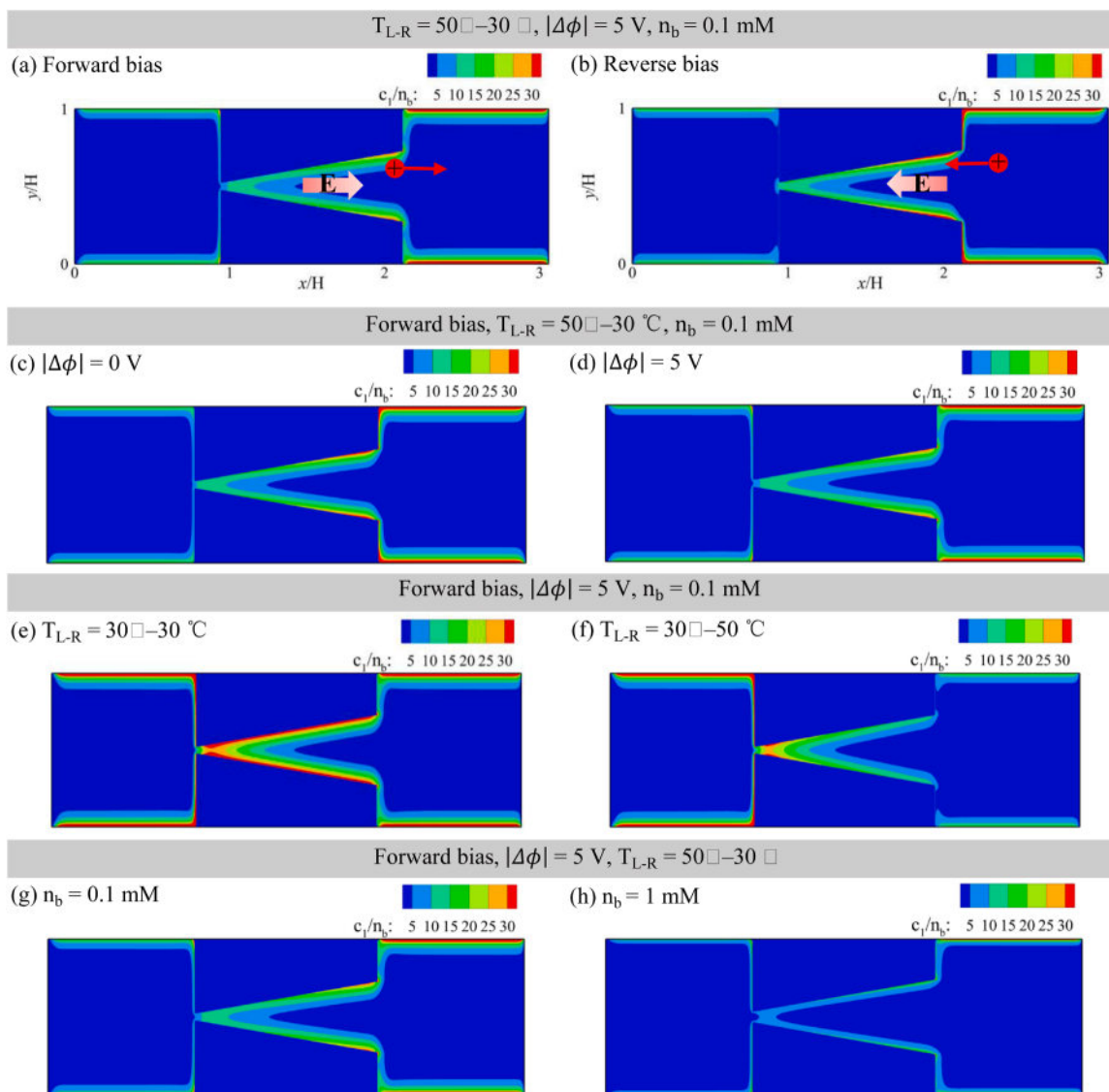


Fig. 4. Contour of counter-ion concentration to demonstrate influence of bias electric field, bulk ionic strength, and temperature gradient on distribution of counterions in nanochannel.

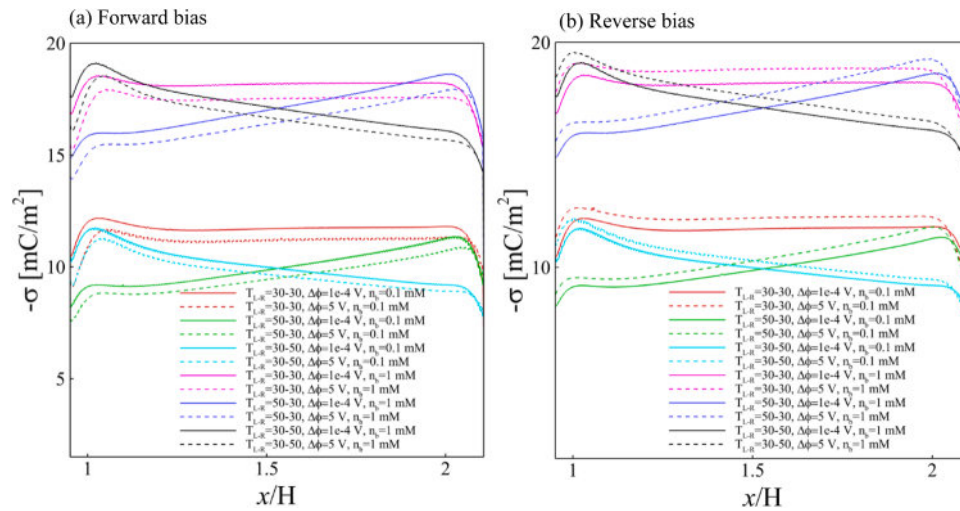


Fig. 5. (a) Forward and (b) reverse bias electrical surface charge versus nanochannel length for different temperature gradients, bulk ionic concentration, and applied external electric field.

code to solve the governing equations coupled with the EQL model equations in FORTRAN. The code has been numerically verified for several previous studies [39,42,46] in terms of comparing the surface charge, zeta potential, ionic concentration, and fluid flow with the available experimental and analytical results.

3. Results and discussion

We solved the governing equations Eqs. (1)–(3) coupled with the proposed temperature-dependent EQL model [39] to obtain $u(x, y)$, $\psi(x, y)$, $c_i(x, y)$, $\zeta(x)$, and $\sigma(x)$. Fig. 3 displays the absolute value of the zeta potential along the nanochannel length for $y = H/2$, where the y -axis is placed on the lower left corner of the system and H denotes the reservoir height (Fig. 1. In Fig. 3, we intentionally presented three applied temperature fields $T_{L-R} = 30^\circ\text{C} - 30^\circ\text{C}$, $T_{L-R} = 50^\circ\text{C} - 30^\circ\text{C}$, and $T_{L-R} = 30^\circ\text{C} - 50^\circ\text{C}$, where the subscript L – R represents the temperature from the left to right reservoir. Note that the applied external electric fields for both forward and reverse bias vary from zero to 5 V. Moreover, we considered two different bulk ion concentrations to study the coupled influence of the temperature gradient, applied electric field, and bulk ion concentration on the physicochemical properties inside the nanofluidic channel as well as the electrokinetic transport phenomena. Fig. 3 indicates that the temperature gradient has a significant influence on the acquired electric potential of the solid-liquid interface. The slope of the absolute value of the zeta potential distant from the tip and base of the nanochannel is directly related to the slope of the temperature variation along the nanochannel ($\frac{d|\zeta|}{dx} \propto \frac{dT}{dx}$), which is consistent with the experimental measurements for a microchannel [33]. Fig. 3 indicates, in general, that temperature has a dominant role in determining the zeta potential. For instance, increasing the bulk ionic strength and temperature have diverse influences that decrease and increase the zeta potential, respectively. Nonetheless, as Fig. 3 indicates, the slope of the zeta potential is determined by the solution temperature. Moreover, our modeling results demonstrate that the zeta potential is not only a function of the solution temperature and bulk ionic strength but also the applied external electric field. Regarding the bulk ionic strength, as expected, by increasing the bulk ionic strength, the absolute value of the zeta potential decreases significantly. This zeta potential behavior was identified by different experimental measurements [50–52]. Regarding the influence of the external electric field, Fig. 3(a) indicates that for the forward bias electric field (electric potential decreasing from tip to base), by increasing the external electric field, the absolute value of the zeta potential increases, whereas for the reverse bias electric field (Fig. 3

(b)), by increasing the applied external electric field, the absolute value of the zeta potential decreases. The modeling results reveal that this behavior of the zeta potential as a function of the applied external electric field is independent of the applied temperature gradient ($\nabla T = 0$ or $\nabla T \neq 0$). This phenomenon can be interpreted by considering the influence of the direction of the applied external electric field on the concentration of counter-ions near the tapered nanochannel walls.

As displayed in Fig. 4(a), the forward bias electric field induces a lower counter-ion concentration near an inclined electrically charged wall because of the pulling of counter-ions away from the nanochannel walls. Conversely, the reverse bias electric field (Fig. 4(b)) induces a greater local counter-ion concentration because of the interaction with the external electric field, which pushes the counter-ions to move closer to the nanochannel walls. Consequently, as mentioned above, by increasing and decreasing the local counter-ion concentration, the absolute value of the zeta potential decreases (reverse bias) and increases (forward bias), respectively. Furthermore, we present the influence of increasing the applied external electric field (Fig. 4(c) and (d)), applying a temperature gradient (Fig. 4(d)–(f)), and increasing the bulk ionic strength (Fig. 4(g) and (h)) by the contour of the counter-ionic species. A comparison of Fig. 4(e) and (f) reveals that the temperature gradient has the most significant influence on the distribution of the counter-ion species inside the nanochannel. Conversely, by increasing the bulk ionic strength, Fig. 4(g) and (h) indicate that the nanochannel bulk region and solution near the nanochannel walls becomes less positively charged.

As mentioned above, the zeta potential at the tip and base of the nanochannel demonstrates nonlinear behavior as a function of the nanochannel length. Considering the tip of the nanochannel, Fig. 3 demonstrates that for all temperature gradients, bulk ionic concentrations, and applied external electric fields, the absolute value of the zeta potential decreases to a local extremum by moving from the tip to base of the nanochannel. In fact, this extremum point can be considered as an energy barrier for ionic species to pass through the tip; nevertheless, this energy barrier is a function of the applied temperature field, which is stronger for $\nabla T > 0$, or that is, when the solution temperature is increasing from the tip to base of the nanochannel. The main reason for the formation of this extremum point at the tip of a tapered nanochannel is explained later.

3.1. Surface charge at solid-liquid interface

The EQL model provides detailed data regarding the EDL properties including the surface charge (σ). Fig. 5 displays the absolute value of the

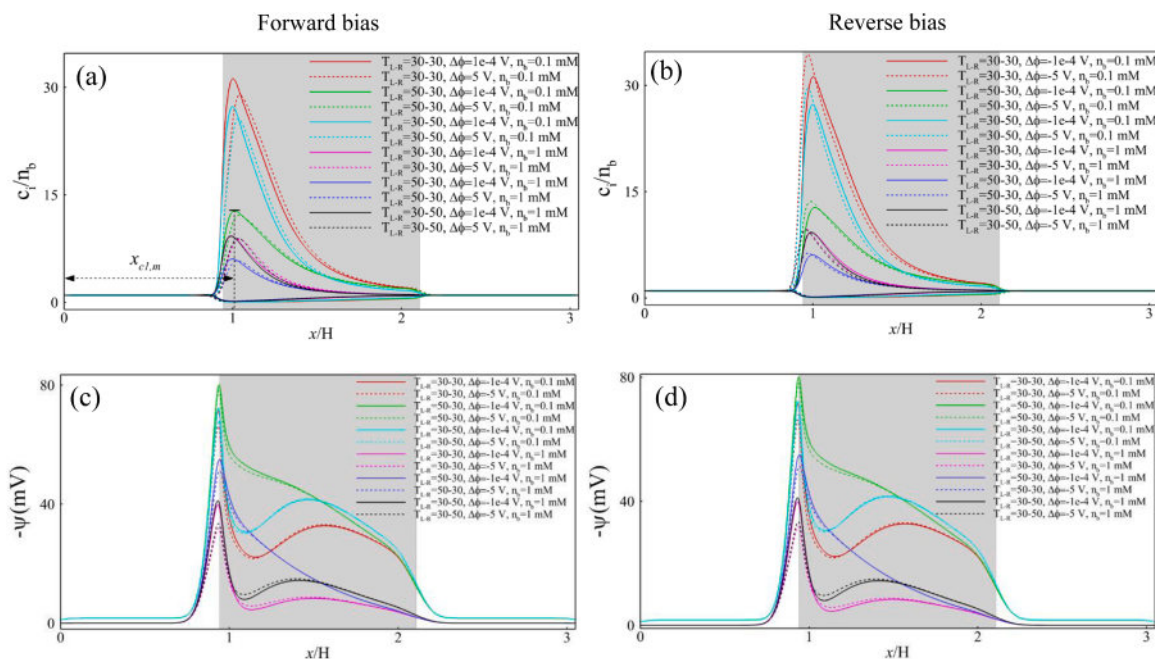


Fig. 6. Normalized concentration of K^+ and Cl^- at centerline and along nanofluidic channel for (a) forward and (b) reverse bias electric fields. The internal electric field at the centerline and along the nanofluidic channel for (c) forward and (d) reverse bias electric fields.

surface charge for the (a) forward and (b) bias-applied electric fields. Similar to the zeta potential, the surface charge is a function of the bulk ionic strength, temperature field, and applied external electric field. Considering the bulk ionic strength, our modeling results demonstrate that by increasing n_b from 0.1 mM to 1 mM, the absolute value of the surface charge increases despite the values of the applied external electric and temperature fields. Moreover, the slope of the surface charge increment along the nanochannel is mainly a function of the applied temperature gradient. For instance, as Fig. 5(a) and (b) indicate, the surface charge on the nanochannel walls (distant from the tip and base) is directly related to the solution temperature ($\nabla\sigma \propto \nabla T$). Furthermore, a comparison of Fig. 5(a) and (b) indicates that the absolute value of the surface charge is a function of the amount and direction of the applied external electric field. To interpret this behavior of the absolute value of the surface charge, we can refer to the same explanation as the zeta potential (Fig. 4). When we apply a forward bias electric field, fewer counter-ions are available near the nanochannel walls and vice versa for the reverse bias electric field. According to the experimental measurements and EDL theories, the acquired surface charge is directly related to the local counter-ion concentration. Consequently, when we apply a forward bias electric field, the local absolute value of the surface charge must be decreased compared to the lower or reverse applied electric fields.

3.2. Ionic concentration and internal electric field

Thus far, we have presented the electrical boundary conditions on nanochannel walls that have a crucial influence on the transport of ionic species through nanofluidic channels [2]. To discuss the temperature gradient on ionic transport through a tapered nanofluidic channel, we must investigate the electrokinetic parameters along the nanochannel. Fig. 6(a) and (b) display the co- and counter-ion concentrations for $c_i(x, H/2)$; the shaded gray area depicts the nanofluidic channel region. As Fig. 6(a) and (b) indicate, the maximum counter-ion concentration is placed inside the nanochannel and near the tip for all temperature field scenarios despite the direction of the applied external electric field (forward or reverse) and bulk ionic strength. However, the maximum peak area of the counter-ion concentration decreases by either

increasing the bulk ionic strength or employing a nonzero temperature field. Considering the bulk ionic strength, this is an expected phenomenon because the selectivity of the nanofluidic channel decreases at the tip owing to a weaker EDL interaction. The temperature gradient has two distinct influences on the peak counter-ion concentration, which depend on the temperature gradient direction. For forward and reverse bias electric fields (Fig. 6(a) and (b)), when a temperature gradient from the base to tip ($\nabla T < 0$) was applied, the maximum amount of the counter-ion concentration at the tip of the nanochannel significantly decreased compared to the isothermal and temperature increasing from the tip to base ($\nabla T > 0$) scenarios. This temperature gradient effect can be explained by recalling the variation in the surface charge on the nanochannel walls (Fig. 5). As discussed above, we demonstrated that the absolute value of the surface charge at the peak area of the nanochannel for $\nabla T < 0$ is the minimum among the other scenarios. Therefore, the concentration of counter-ions that can be attracted to the tip of the nanochannel to balance the acquired surface charge on the nanochannel walls is decreased. Considering the influence of the strength and direction of the applied external electric field, Fig. 6(a) and (b) indicate that by increasing the applied bias electric field, the extremum point of the counter-ion concentration at the centerline of the nanochannel is moved to the base of the nanochannel for the forward bias electric field, whereas it approaches the tip of the nanochannel for the reverse bias electric field. Furthermore, applying higher electric fields influences the extremum of the counter-ion concentration curve at the tip of the nanochannel such that the forward bias electric field decreases the accumulation of counter-ion concentration, whereas the reverse bias electric field increases beyond the lower applied external electric fields.

The electric field ($\psi(x, H/2)$) induced by the EDL is indicated for forward (Fig. 6(c)) and reverse (Fig. 6(d)) bias electric fields. Interestingly, at the centerline of a tapered nanochannel, the energy barrier that we discussed for the zeta potential (Fig. 3) appears, which is stronger for the isothermal and $\nabla T > 0$ temperature fields. For $\nabla T < 0$, our modeling results indicate that the absolute value of the internal electric potential inside the nanochannel is always decreasing. This means that $\nabla T < 0$ eliminates the energy barrier inside the tapered nanofluidic channel, which induces a stable internal electric field variation from the base to tip of the nanochannel. Consequently, the induced internal electric field,

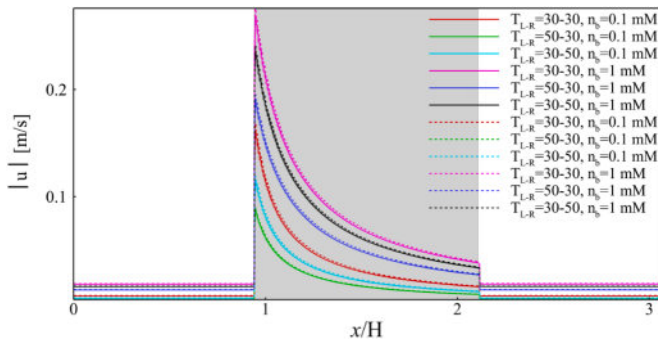


Fig. 7. Absolute value of electroosmotic velocity through nanochannel for forward (solid lines) and reverse (dashed lines) bias electric fields with $|\Delta\phi|=5$ V.

which is mainly independent of the forward or reverse bias electric field, weakens or strengthens the influence of the external electric field. Later, we discuss the extent to which this phenomenon influences the ionic current through the nanofluidic channel.

As expected, by increasing the bulk ionic strength, the absolute value of the internal electric potential decreases, which is a consequence of the decrease in zeta potential due to the increase in the bulk ionic strength (Fig. 3). Moreover, the internal electric potential for isothermal ($30^\circ\text{C} - 30^\circ\text{C}$) and $\nabla T > 0$ ($30^\circ\text{C} - 50^\circ\text{C}$) at the tip of the nanochannel is approximately the same because of the reduced selectivity of the nanochannel tip at a lower solution temperature (lower zeta potential and therefore weaker EDL interaction).

3.3. Electroosmotic velocity

In the previous sections, we presented the influence of the temperature gradient as well as the applied external electric field and bulk ionic strength on the distribution of the ionic species and internal electric potential field (Fig. 6). The other parameter that has a role in the ionic current is the electroosmotic velocity, which is obtained by solving the Navier–Stokes equations (Eq. (6)). Fig. 7 displays the absolute value of the electroosmotic velocity versus the nanochannel length for forward (solid line) and reverse (dashed line) bias electric fields under the influence of diverse temperature fields and bulk ionic strengths, wherein as in Fig. 6, the shaded gray area represents the tapered nanochannel. For all scenarios, the electroosmotic velocity sharply increased at the tip of the nanochannel, which is reasonable because the cross-sectional area decreases from the reservoir to the tip. Interestingly, the electroosmotic flow could be significantly manipulated by the applied temperature gradient. Our modeling results reveal that for a solution with $\nabla T < 0$, the electroosmotic velocity decreased more than with $\nabla T > 0$. This behavior of the nanochannel can be interpreted by considering the zeta potential and internal electric field, which we presented in Figs. 3, 6(c) and (d). To explain this behavior of the electroosmotic flow, we consider the simple one-dimensional analytical solution of the Navier–Stokes equation (Eq. (6)) and non-slip boundary conditions on the channel walls [53,54]

$$u(y) = -\frac{\epsilon_0 \epsilon_r E}{\mu} \zeta \left[1 - \frac{\cosh(\kappa y)}{\cosh(\kappa H)} \right], \quad (7)$$

where $\kappa = \sqrt{\left(\frac{2e^2 n_b}{\epsilon_0 \epsilon_r k_B T} \right)}$ denotes the inverse of the EDL characteristic length [55]. Whereas solving Eq. (7) for different amounts of zeta potential and channel height indicates that the electroosmotic velocity increases by increasing the height of the nanochannel or decreasing the bulk ionic strength [45]; conversely, increasing the absolute value of the zeta potential increases the characteristic length of the EDL. Consequently, the electroosmotic velocity is decreased. Although the present

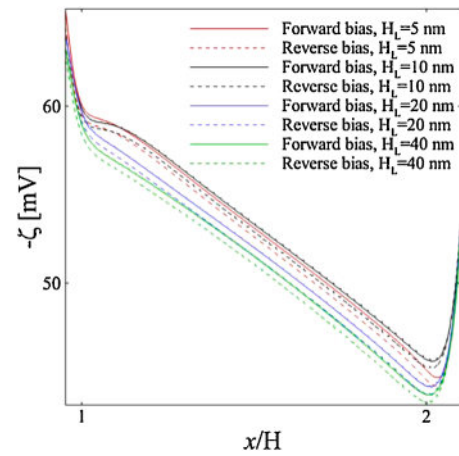


Fig. 8. Influence of nanochannel height on zeta potential for bulk reservoir concentration $n_b = 1$ mM, $T_L - R = 50^\circ\text{C} - 30^\circ\text{C}$, $|\Delta\phi|=0.5$ V, and $n_b = 1$ mM.

study focuses on the nanochannels with low ionic strength which justifies the overlapping of the EDL, but Eq. (7) can still provide the trend of EOF velocity with the channel parameters such as height and zeta potential. Fig. 7 indicates the same trend, wherein for $\nabla T < 0$ and a specified bulk ionic strength, the electroosmotic velocity has a minimum amount compared to the isothermal and $\nabla T > 0$ scenarios. Note that the minimum amount of the electroosmotic velocity belongs to the smaller bulk ionic strength with $\nabla T < 0$, where we have the maximum absolute value of the zeta potential and internal electric field (Figs. 3 and 6). The maximum electroosmotic velocity can be obtained by increasing the bulk ionic strength and applying an isothermal temperature field (electroosmotic velocity for $n_b = 1$ mM and $\nabla T = 0$). Regarding the influence of the bias electric field direction, Fig. 7 indicates that we can assume that the absolute value of the electroosmotic velocity is an independent parameter of the forward or reverse bias electric fields.

3.4. Influence of nanochannel height

We have demonstrated that the temperature gradient and bulk ionic strength can significantly influence the physicochemical properties of tapered nanochannels. One influential phenomenon that determines the ion selectivity of a nanochannel is the overlapping of the EDLs. The overlapping of the EDLs could occur by decreasing the nanochannel height, decreasing the bulk ionic strength, or increasing the solution temperature. In this section, we aim to vary the tip height while retaining the nanochannel inclination angle ($\theta = 10^\circ$). Fig. 8 displays the zeta potential for nanochannels with $H_L=5, 10, 20,$ and 40 nm, which were subjected to $T_L - R = 50^\circ\text{C} - 30^\circ\text{C}$, $|\Delta\phi|=0.5$ V, and $n_b=1$ mM. The modeling results indicate that the zeta potential did not change significantly when we increased the tip height from 5 to 10 nm, whereas further increasing the tip height to 20 and 40 nm significantly decreased the absolute value of the zeta potential. This trend of the zeta potential can be explained by considering the overlapping of the EDL, which can be identified by determining the ratio of the EDL thickness and tip height as $\kappa H_L \rightarrow 5\text{nm} = 0.52$, $\kappa H_L \rightarrow 10\text{nm} = 1.05$, $\kappa H_L \rightarrow 20\text{nm} = 2.1$, and $\kappa H_L \rightarrow 40\text{nm} = 4.2$. As Fig. 9(a) indicates, for fully overlapped EDLs ($\kappa H_L = 0.52$ and 1.05), by decreasing the tip height from 10 to 5 nm, the counter-ion concentration did not change as significantly as when the tip height varied from 20 to 10 nm. This finding supports the argument that by further decreasing the tip height, there is not a significant change in counter-ion concentration; therefore, the zeta potential remains approximately unchanged. As we have previously alluded to the source of internal electric potential, Fig. 9(b) indicates that following the counter-ion concentration behavior for tip heights of 5 and 10 nm, the internal electric potential does not significantly change ($\frac{\psi_{H_L=5\text{nm}}}{\psi_{H_L=10\text{nm}}} = 1.14$)

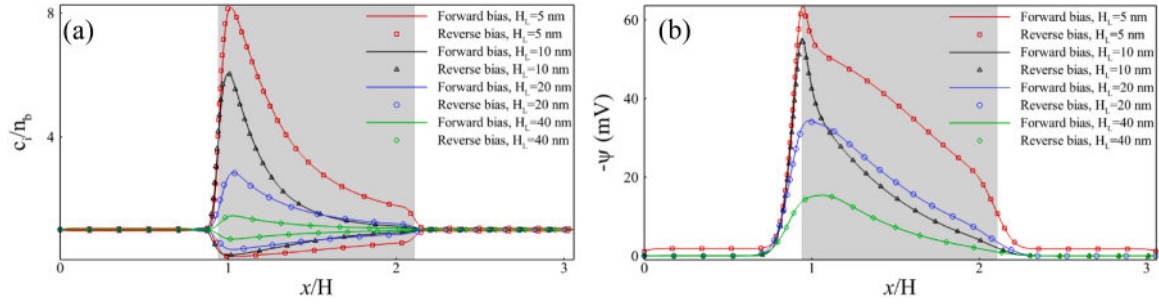


Fig. 9. Centerline amounts of (a) normalized concentration of K^+ and Cl^- and (b) $-\psi$ (mV) along nanochannels with tip heights of $H_t = 5$ nm, 10 nm, 20 nm, and 40 nm for bulk reservoir concentration $n_b = 1$ mM, $T_{L-R} = 50^\circ C-30^\circ C$, $|\Delta\phi| = 0.5$ V, and $n_b = 1$ mM.

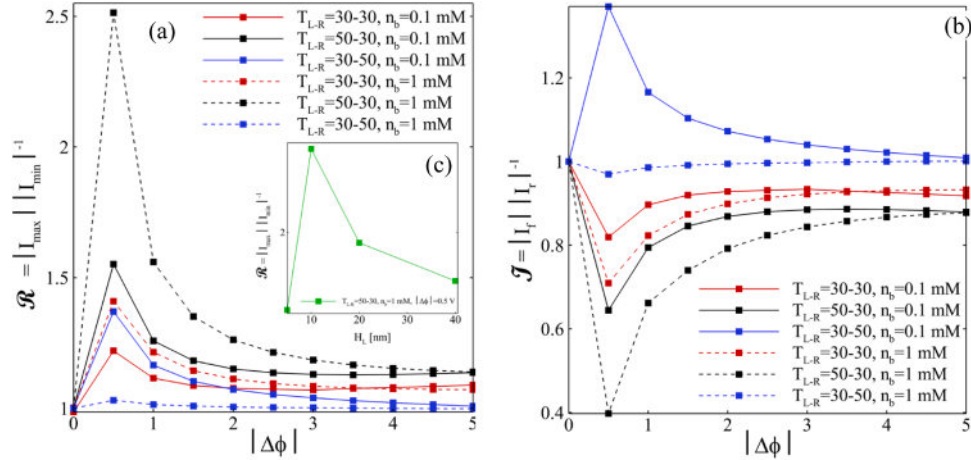


Fig. 10. (a) Ionic rectification ratio (\mathcal{R}) and (b) ratio (\mathcal{S}) of absolute value of forward ($|I_f|$) to reverse ($|I_r|$) ionic current for three temperature fields ($\nabla T = 0$, $\nabla T > 0$, and $\nabla T < 0$) and for two ionic strength ($n_b = 0.1$ mM and $n_b = 1$ mM). (c) the influence of the nanochannel tip height on \mathcal{R} for $H_t = 5, 10, 20$, and 40 nm.

at the tip of the nanochannel compared to the 20 and 40 nm ($\frac{\psi_{H_t=20nm}}{\psi_{H_t=40nm}} = 2.36$) scenarios.

3.5. Ionic current and rectification ratio

The ionic current through the nanochannel is triggered by the advection, diffusion, and electromigration of the ions, which is defined as

$$I(x) = w \int_{\frac{-H(x)}{2}}^{\frac{H(x)}{2}} \left\{ u \sum_i e z_i c_i - e \sum_i D_i z_i \nabla c_i - e \nabla (\bar{\psi} + \bar{\phi}) \sum_i z_i^2 D_i c_i \right\} dy, \quad (8)$$

where w , $H(x)$, and u denote the width of the nanochannel ($w = 60\mu m$), height of the nanochannel ($H(x) = H_L + x \tan(\theta)$), and fluid flow velocity along the nanochannel length, respectively. We can rewrite Eq. (8) as

$$I(x) = w \int_{\frac{-H(x)}{2}}^{\frac{H(x)}{2}} \left\{ u \rho_e - \tilde{D} \nabla \rho_e - \tilde{D} \nabla (\bar{\psi} + \bar{\phi}) \sum_i e z_i^2 c_i \right\} dy, \quad (9)$$

By introducing the definition of the net electric charge density ($\rho_e = \sum_i e z_i c_i$) into Eq. (8) and defining the average ionic diffusion coefficient $\tilde{D} = \frac{D_{K^+} + D_{Cl^-}}{2}$. The first term on the right-hand side of Eq. (9) represents the ionic current due to advection, the second term represents the diffusion, and the last term represents the ionic current due to electromigration. Using Eq. (9) to calculate the ionic current for different temperatures and applied external electric fields, we can obtain the rectification ratio

(\mathcal{R}), which is defined as

$$\mathcal{R} = |I_{max}| |I_{min}|^{-1}. \quad (10)$$

Furthermore, we were interested in the direction of the maximum ionic current. Thus, we define the ratio of the forward ionic current to the reverse as

$$\mathcal{S} = |I_f| |I_r|^{-1}. \quad (11)$$

Fig. 10(a) displays the rectification ratios and Fig. 10(b) indicates the ratio of forward to reverse ionic current versus the absolute value of the applied potential difference ($|\Delta\phi|$) for three temperature fields and two bulk ionic strengths. As Fig. 10(a) and (b) indicate, the applied temperature gradients can significantly manipulate the rectification ratio of the tapered nanofluidic channel. Note that by increasing the bulk ionic strength, the influence of the temperature gradient on the rectification ratio is strengthened (comparing the isochromatic solid and dashed lines). Interestingly, the direction of the applied temperature gradient could significantly increase or decrease the ionic rectification ratio. For instance, if we apply a decreasing solution temperature from the tip to base of the nanochannel ($\nabla T < 0$), our modeling results reveal that the rectification ratio is significantly enhanced compared to other applied temperature fields ($\nabla T = 0$ and $\nabla T > 0$) with the same bulk ionic strength (solid and dashed lines in Fig. 10(a)). Furthermore, by increasing the bulk ionic strength, the increasing solution temperature from the tip to base ($\nabla T > 0$) demonstrates a reverse influence on rectification ratio compared to $\nabla T = 0$ and $\nabla T < 0$. As Fig. 10(a) indicates, for greater bulk ionic strength, the increasing temperature from the tip to base (dashed blue line) suppresses the ionic rectification property of the tapered nanochannel, which is even less than the rectification ratio of the isothermal scenario (dashed red line). This

significant influence of the direction of the temperature gradient can be reversed when we apply a decreasing solution temperature from the tip to base ($\nabla T < 0$, black dashed line), which increases the rectification ratio by 2.5 compared to the same bulk ionic strength ($n_b = 1$ mM) with $\nabla T > 0$.

Considering the ratio of the forward to reverse ionic current, Fig. 10 (b) indicates that the maximum ionic current occurs mainly in the reverse direction, except for the solution with $\nabla T > 0$ and $n_b = 0.1$ mM (blue solid line).

As mentioned previously (Eq. (8)), three transport phenomena are responsible for generating an ionic current, which is represented as (i) advection $\rho_e u$, (ii) diffusion $\bar{D}\nabla\rho_e$, and (iii) electromigration $\bar{D}\nabla(\bar{\psi} + \bar{\phi}) \sum ez_i^2 n_i$. A simple dimensional analysis of the three ionic current terms indicates that for the tip of the nanochannel, the order of the advection and electromigration terms is $\mathcal{O}(u\rho_e) = \mathcal{O}(\bar{D}\nabla(\bar{\psi} + \bar{\phi}) \sum ez_i^2 n_i) \sim 10^4$, whereas the order of the diffusion terms is $\mathcal{O}(\bar{D}\nabla\rho_e) = \sim 10^3$. Although the contribution of the advection term in the ionic current is on the order of the electromigration term, the nonsignificant influence of the electrical bias direction on the electroosmotic velocity (Fig. 7) and net electric charge density (Fig. 6(a) and (b)) justifies the argument that the rectification ratio of the nanochannel can be determined based on the competition between the diffusion and electromigration terms. On the other word, the ionic rectification behavior of the present work nanochannel will be solely determined based on the contribution of two other transport phenomena which are diffusion and electromigration. Therefore, a simple analysis based on the ionic concentrations (Fig. 6(a) and (b)) and internal electric field (Fig. 6(c) and (d)) indicates that for the forward bias electric field ($\nabla\phi < 0$) and reverse bias electric field ($\nabla\phi > 0$), we have $\nabla\psi|_{x < x_{\psi,m}} > 0$ and $\nabla\psi|_{x > x_{\psi,m}} < 0$, where $x_{\psi,m}$ denotes the extremum point for the internal electric field inside the nanochannel. The contribution of the electromigration term in ionic current depends on the applied external electric field, which could be $|\nabla(\bar{\psi} + \bar{\phi})_f| = |\nabla(\bar{\psi} + \bar{\phi})_r|$ for $\nabla\phi = 0$ and $|\nabla(\bar{\psi} + \bar{\phi})_f| < |\nabla(\bar{\psi} + \bar{\phi})_r|$ or $|\nabla(\bar{\psi} + \bar{\phi})_f| > |\nabla(\bar{\psi} + \bar{\phi})_r|$ for $\nabla\phi \neq 0$. Selecting the highest applied electric field in this contribution ($|\Delta\phi| = 5$ V), clearly, the contribution of the electromigration in the reverse bias electric field is greater than the forward the bias electric field, which means that $|\nabla(\bar{\psi} + \bar{\phi})_f| < |\nabla(\bar{\psi} + \bar{\phi})_r|$. Moreover, as indicated in Fig. 6 (a) and (b), we have a greater amount of $\sum ez_i^2 n_i$ for the reverse bias electric field compared to the forward bias. Therefore, the contribution of the electromigration term in the reverse bias electric field is greater than that in the forward bias. Regarding the diffusion contribution in the ionic current, Fig. 6(a) and (b) demonstrate that $\nabla\rho_e|_{x < x_{c_1,m}} > 0$ and $\nabla\rho_e|_{x < x_{c_1,m}} < 0$, where $x_{c_1,m}$ represents the extremum point for the counter-ion concentration inside the nanochannel. Conversely, the gradient of the net electric charge density for forward and bias electric fields are $\nabla\rho_{ef} < \nabla\rho_r$. Therefore, the contribution of the diffusion in the reverse bias electric field is more significant than that in the forward bias electric field.

Considering the influence of tip height on the ionic rectification behavior of the nanochannel, Fig. 10(c) indicates that by increasing H_L from 5 to 10 nm, \mathcal{R} increases from 1.5 to 2.5, and further increasing H_L to 20 and 40 nm, the rectification ratio decreases to 1.93 and 1.7, respectively. Consequently, it can be deduced that decreasing the tip height of a tapered nanochannel does not always increase the rectification ratio. To interpret this behavior of nanochannels with $H_L = 20$ and 40 nm, Fig. 9(a) and (b) indicate that by increasing the height of the nanochannel beyond 10 nm, wherein the EDLs do not overlap at the tips, the value of $\nabla\psi$ and $\nabla\rho_e$ for $x > x_m$ is decreasing. Therefore, the ionic current in the reverse bias electric field decreases and finally decreases the rectification of the ionic current. Unlike the non-overlapped regime, for the overlapped EDL regime, increasing the tip height from $H_L = 5$ to 10 nm increases the ionic rectification of the nanochannel. Our

modeling results (Fig. 9(b)) revealed the interesting fact that $\nabla\psi$ inside the nanochannel is greater for $H_L = 10$ nm. Therefore, the contribution of the electromigration term is greater than that of $H_L = 5$ nm.

4. Semi-analytical solution

In this section, we propose a simple one-dimensional (1D) semi-analytical solution to understand the physics underlying ion transport through a tapered nanochannel with a temperature gradient. As mentioned in the previous section, the ionic current rectification behavior is determined based on the interplay of the diffusion and electromigration transport phenomena. Consequently, it is reasonable to neglect the convection term $u\rho_e$ in the proposed semi-analytical solution and simplify the steady-state Nernst-Planck equations for both counter- and co-ions as

$$\begin{aligned} a) : \text{Counter-ion} : 0 &= \nabla^2 c_1 + \nabla \cdot [c_1 \nabla (\bar{\psi} + \bar{\phi})], \\ b) : \text{Co-ion} : 0 &= \nabla^2 c_2 - \nabla \cdot [c_2 \nabla (\bar{\psi} + \bar{\phi})]. \end{aligned} \quad (12)$$

If we sum Eq. (12) a and b and define $n_s = \frac{(c_1+c_2)}{2}$ and $n_d = \frac{(c_1-c_2)}{2}$, we have

$$0 = \nabla^2 n_s + \nabla \cdot [n_d \nabla (\bar{\psi} + \bar{\phi})]. \quad (13)$$

Because we are studying a tapered nanofluidic channel, the zero flux of the ionic species along the y-direction is no longer valid. However, the zero-flux condition remains available perpendicular to the nanochannel walls, which justifies employing the $n-t$ (normal-tangential coordinate) as the reference coordinate that stands on the lower nanochannel wall. Hence, Eq. (13) can be written as

$$\begin{aligned} 0 &= \frac{\partial^2 n_s}{\partial n^2} + \frac{\partial^2 n_s}{\partial t^2} + \frac{\partial n_d}{\partial n} \left(\frac{\partial (\bar{\psi} + \bar{\phi})}{\partial n} \right) + n_d \left(\frac{\partial^2 (\bar{\psi} + \bar{\phi})}{\partial n^2} \right) \\ &+ \frac{\partial n_d}{\partial t} \left(\frac{\partial (\bar{\psi} + \bar{\phi})}{\partial t} \right) + n_d \left(\frac{\partial^2 (\bar{\psi} + \bar{\phi})}{\partial t^2} \right). \end{aligned} \quad (14)$$

Recalling the zero-flux of ionic species normal to the nanochannel walls, we have two relations

$$\begin{aligned} J_{1,n} = 0 &\rightarrow \frac{\partial c_1}{\partial n} + c_1 \frac{\partial (\bar{\psi} + \bar{\phi})}{\partial n} = 0, \\ J_{2,n} = 0 &\rightarrow \frac{\partial c_2}{\partial n} - c_2 \frac{\partial (\bar{\psi} + \bar{\phi})}{\partial n} = 0. \end{aligned} \quad (15)$$

If we sum Eq. (15) a and b, then we have

$$J_{1,n} + J_{2,n} = 0 \rightarrow \frac{\partial n_s}{\partial n} + n_d \frac{\partial (\bar{\psi} + \bar{\phi})}{\partial n} = 0. \quad (16)$$

Taking the gradient of Eq. (16) ($\nabla(J_{1,n} + J_{2,n})$) and introducing the result into Eq. (14), we obtain

$$0 = \frac{\partial^2 n_s}{\partial t^2} + \frac{\partial n_s}{\partial t} \left(\frac{\partial (\bar{\psi} + \bar{\phi})}{\partial t} \right) + n_s \left(\frac{\partial^2 (\bar{\psi} + \bar{\phi})}{\partial t^2} \right). \quad (17)$$

Considering the lower half of the nanochannel, we can relate the differential in the t -direction to the x - and y -directions as $dx = (\cos\theta)dt$ and $dy = (\sin\theta)dt$. If we introduce these relations into Eq. (17), we have two separate mass conservation equations in the x - and y -directions. For the x -direction, we introduce the former relation and the dimensionless format of the parameters $\bar{y} = \frac{y}{H_L}$, $\bar{x} = \frac{x}{L}$, $\bar{n} = \frac{n}{n_b}$, and $\bar{\psi} = \psi/V_t$ to Eq. (17) yielding

$$0 = \frac{\partial^2 \bar{n}_s}{\partial \bar{x}^2} + \frac{\partial \bar{n}_s}{\partial \bar{x}} \left(-\frac{EL}{V_t} + \frac{\partial \bar{\psi}}{\partial \bar{x}} \right) + \bar{n}_d \frac{\partial^2 \bar{\psi}}{\partial \bar{x}^2}. \quad (18)$$

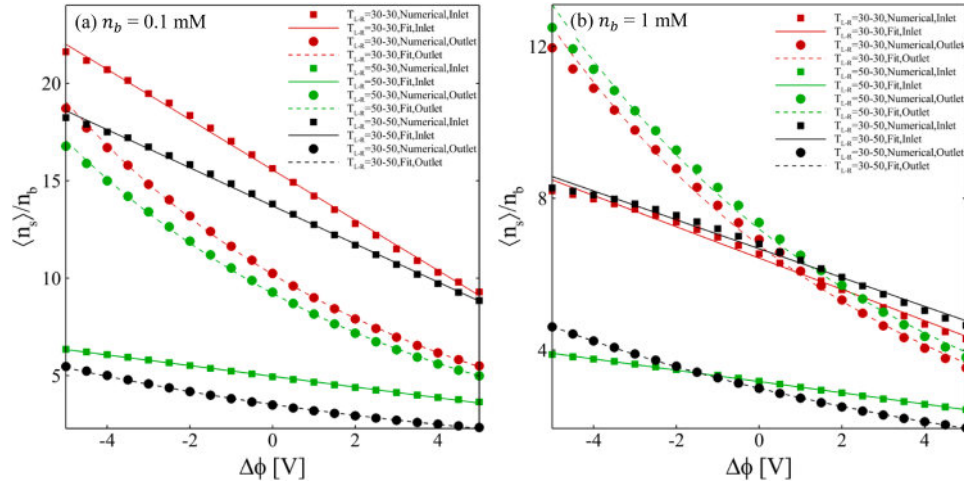


Fig. 11. Non-dimensionalized $\langle \bar{n}_s \rangle$ versus applied external electric potential for ionic strengths (a) $n_b = 0.1$ mM and (b) $n_b = 1$ mM. The circle and square symbols represent the outlet and inlet amounts of $\langle \bar{n}_s \rangle$ from our numerical modeling, respectively, whereas the lines (dashed and solid) represent the fitting curves.

Note that the mass conservation equation can be solved in the y -direction, as we have a locally nonzero flux of ionic species. However, the integral of the cross-sectional y -direction ionic fluxes is zero because of the symmetry (the ionic fluxes in the y -direction for the upper and lower parts of the nanochannel cancel each other). To simplify Eq. (18), we assume that the tapered nanofluidic channel is covered with overlapped EDLs. Clearly, the overlapping of the EDLs is considerably stronger at the tip than at the base of the nanochannel. This assumption occurs in a 1D Poisson equation (Eq. (2)), which is written as $\frac{\partial^2 \bar{\psi}}{\partial \bar{x}^2} = -\frac{\rho_e L^2}{V_t \epsilon}$. If we integrate from both sides of this 1D Poisson equation along the nanochannel cross section and define

$$\langle \bar{\psi} \rangle = \frac{\int_0^{\bar{H}(\bar{x})} \bar{\psi} d\bar{y}}{\bar{H}(\bar{x})} \quad (19)$$

then, we have

$$\langle \bar{n}_d \rangle = -\frac{V_t \epsilon}{en_b L^2} \frac{d^2 \langle \bar{\psi} \rangle}{d\bar{x}^2}, \quad (20)$$

where $\bar{H}(\bar{x}) = 1 + \left(\tan(\theta) \frac{L}{H_t} \right) \bar{x}$.

To eliminate any complexity due to solving coupled differential equations, we assume that

$$\bar{\psi} = \bar{\zeta} \exp\left(-\kappa H_L (\bar{H}(\bar{x}) - \bar{y})\right), \quad (21)$$

where

$$\langle \bar{\psi} \rangle = \frac{\bar{\zeta}}{\bar{H}(\bar{x}) H_L \kappa} \left[\exp\left(-\kappa H_L \bar{H}(\bar{x})\right) - 1 \right]. \quad (22)$$

where for $n_b = 0.1$ mM, we have $\zeta = 10^{-3}(-0.06T - 107.4)$, and for $n_b = 1$ mM, the zeta potential is $\zeta = 10^{-3}(-0.44T - 78.2)$ according to the experimental measurements [33]. In Eq. (22) we non-dimensionalize the zeta potential with the thermal voltage as $\bar{\zeta} = \zeta/V_t$, where $V_t = k_B T_{ave}/e$ and $T_{ave} = 0.5(T_L + T_R) + 273.15$ K. Considering the temperature distribution, we assume that the temperature is $T(\bar{x}) = T_L + (T_R - T_L)\bar{x}/L$. To provide a 1D model, we integrate Eq. (18) through the cross section

of the tapered nanochannel and define $\langle \bar{n}_s \rangle = \frac{\int_0^{\bar{H}(\bar{x})} \bar{n}_s d\bar{y}}{\bar{H}(\bar{x})}$ and $\langle \bar{n}_d \rangle =$

$$\frac{\int_0^{\bar{H}(\bar{x})} \bar{n}_d d\bar{y}}{\bar{H}(\bar{x})}, \text{ yielding}$$

Table 1
 $\langle \bar{n}_s \rangle$ Fitting functions for temperature fields and bulk ionic strengths.

	Temperature (°C)	$n_b = 0.1$ mM	$n_b = 1$ mM
Inlet $\bar{x} = 0$	$T_L = 30, T_R = 30$	$\langle \bar{n}_s \rangle = -1.2891\Delta\phi + 15.557$	$\langle \bar{n}_s \rangle = -0.4123\Delta\phi + 6.424$
	$T_L = 50, T_R = 30$	$\langle \bar{n}_s \rangle = -0.2746\Delta\phi + 4.9645$	$\langle \bar{n}_s \rangle = -0.1488\Delta\phi + 3.171$
	$T_L = 30, T_R = 50$	$\langle \bar{n}_s \rangle = -0.9771\Delta\phi + 13.711$	$\langle \bar{n}_s \rangle = -0.3804\Delta\phi + 6.6717$
Outlet $\bar{x} = 1$	$T_L = 30, T_R = 30$	$\langle \bar{n}_s \rangle = 10.195e^{-0.125\Delta\phi}$	$\langle \bar{n}_s \rangle = 6.7614e^{-0.123\Delta\phi}$
	$T_L = 50, T_R = 30$	$\langle \bar{n}_s \rangle = 9.2211e^{-0.123\Delta\phi}$	$\langle \bar{n}_s \rangle = 7.1892e^{-0.12\Delta\phi}$
	$T_L = 30, T_R = 50$	$\langle \bar{n}_s \rangle = 3.5199e^{-0.086\Delta\phi}$	$\langle \bar{n}_s \rangle = 2.991e^{-0.087\Delta\phi}$

$$\frac{d^2 \langle \bar{n}_s \rangle}{d\bar{x}^2} = -\left(\frac{1}{\bar{H}(\bar{x})} \right) \left(-\frac{EL}{V_t} + \frac{d\langle \bar{\psi} \rangle}{d\bar{x}} \right) \frac{d\left(\bar{H}(\bar{x}) \langle \bar{n}_d \rangle \right)}{d\bar{x}} - \frac{d^2 \langle \bar{\psi} \rangle}{d\bar{x}^2} \langle \bar{n}_d \rangle. \quad (23)$$

Introducing the relations for $\langle \bar{\psi} \rangle$ and $\langle \bar{n}_d \rangle$ into Eq. (23) yields $\frac{d^2 \langle \bar{n}_s \rangle}{d\bar{x}^2} = f(\bar{H}(\bar{x}), a \exp(b\bar{x} + c) + d)$, where the right-hand side is a complex function of the nanochannel width and an exponential function. This differential equation cannot be analytically solved. To address this challenge, we found that the right-hand side of Eq. (23) can be approximated by an exponential function $f(\bar{H}(\bar{x}), a \exp(b\bar{x} + c) + d) \approx a_1 \exp(b_1 \bar{x} + c_1)$, where $a_1, b_1,$ and c_1 are obtained by least squares fitting with the original function f . This fitting permits us to solve Eq. (23) analytically, yielding

$$\langle \bar{n}_s \rangle = \frac{a_1}{b_1^2} \exp(b_1 \bar{x} + c_1) + C_1 \bar{x} + C_2, \quad (24)$$

with the boundary conditions $\langle \bar{n}_s \rangle_{\bar{x}=0} = \alpha, \langle \bar{n}_s \rangle_{\bar{x}=1} = \beta$, which we borrowed from our numerical model. Fig. 11 represents the $\langle \bar{n}_s \rangle$ for (a) $n_b = 0.1$ mM and (b) $n_b = 1$ mM, as well as the fitting functions in Table 1. Several interesting points can be inferred: (i) the value of $\langle \bar{n}_s \rangle$ at the tip of a tapered nanochannel demonstrates a linear relation with the applied potential difference for all temperature fields and ionic strength scenarios; (ii) the values of $\langle \bar{n}_s \rangle$ at the base of the nanochannel are exponential functions of the applied electric potential difference; (iii) for both ionic strength scenarios, it has been demonstrated that applying

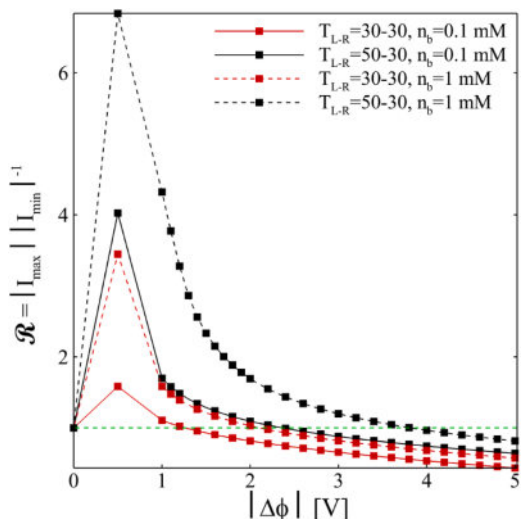


Fig. 12. Rectification ratio (\mathcal{R}) is based on solving Eq. (25) for the entire nanochannel.

temperature gradient $\nabla T < 0$ makes the tip of the nanochannel less sensitive to the applied potential difference, which results in (iv) increasing the $\langle \bar{n}_s \rangle_{\bar{x}=1} - \langle \bar{n}_s \rangle_{\bar{x}=0}$ from a forward bias electric field.

Because we already have $\langle \bar{n}_s \rangle$ (Eq. (24)) and $\langle \bar{n}_d \rangle$ (Eq. (20)), we can determine the ionic current as

$$I(x) = -\frac{4w\tilde{D}_eH_L}{L}n_b \left(\frac{d\langle \bar{H}(\bar{x}) \rangle \langle \bar{n}_d \rangle}{d\bar{x}} + \left(\frac{-EL}{V_i} + \frac{d\langle \bar{\psi} \rangle}{d\bar{x}} \right) \langle \bar{H}(\bar{x}) \rangle \langle \bar{n}_s \rangle \right). \quad (25)$$

Fig. 12 displays the ionic rectification ratio \mathcal{R} obtained by averaging the ionic current (Eq. (25)) over the length of the nanochannel versus the applied external potential difference. It has been demonstrated that the proposed semi-analytical solution predicts the rectification ratios on the same order of magnitude and trend as the numerical results (Fig. 10 (a)). As indicated in Fig. 12, for a greater applied electrical potential, Eq. (25) predicts rectification ratios less than one (beneath the dashed green line in Fig. 12). This prediction contradicts the numerical rectification ratio, which can be explained by considering the simplifying assumptions related to the zeta potential and 1D Poisson equation.

5. Conclusions

In this study, we theoretically demonstrated that a temperature-regulated surface charge can manipulate the ionic rectification of a single-material tapered nanochannel. Our modeling results indicate that the ionic current can be actively manipulated by applying temperature gradients from the tip to base and vice versa while changing the bulk ionic strength and tip height. The key influence of temperature and bulk ionic strength on the surface charge and therefore, on the ionic current, was determined by calculating the surface charge and zeta potential based on a temperature-dependent EDL model. It was revealed that applying a decreasing temperature from the tip to base associated with a greater bulk ionic strength could significantly enhance the ionic rectification ratio of the nanochannel, whereas applying a temperature gradient in the reverse direction significantly suppressed the rectification behavior of the nanochannel. Moreover, we demonstrated that the rectification behavior of the tapered nanochannel is mainly determined by the overlapping of the EDLs at the tip of the nanochannel. Finally, we developed a semi-analytical solution and obtained a rectification ratio that supported the numerical modeling results with the same order of magnitude and corroborated our argument that the surface charge inhomogeneity due to the temperature gradient could significantly

enhance the rectification ratio.

CRedit authorship contribution statement

Amer Alizadeh: Investigation, Software, Validation, Writing – original draft. **Wei-Lun Hsu:** Validation, Writing – review & editing. **Hirofumi Daiguji:** Supervision, Writing – review & editing. **Moran Wang:** Conceptualization, Supervision, Writing – review & editing, Project administration.

Declaration of Competing Interest

The authors declare that they have no known competing financial interests or personal relationships that could have appeared to influence the work reported in this paper.

Acknowledgment

This work was financially supported by the National Natural Science Foundation of China (No.51676107, 51176089) and the UTokyo-Tsinghua Collaborative Research Fund.

Supplementary materials

Supplementary material associated with this article can be found, in the online version, at [doi:10.1016/j.ijmecsci.2021.106754](https://doi.org/10.1016/j.ijmecsci.2021.106754).

References

- [1] Schoch RB, Han JY, Renaud P. Transport phenomena in nanofluidics. *Rev Mod Phys* 2008;80(3):839–83.
- [2] Stein D, Kruihof M, Dekker C. Surface-charge-governed ion transport in nanofluidic channels. *Phys Rev Lett* 2004;93(3):4.
- [3] Karnik R, Castelino K, Fan R, Yang P, Majumdar A. Effects of biological reactions and modifications on conductance of nanofluidic channels. *Nano Lett* 2005;5(9):1638–42.
- [4] Karnik R, Fan R, Yue M, Li DY, Yang PD, Majumdar A. Electrostatic control of ions and molecules in nanofluidic transistors. *Nano Lett* 2005;5(5):943–8.
- [5] Daiguji H, Yang PD, Majumdar A. Ion transport in nanofluidic channels. *Nano Lett* 2004;4(1):137–42.
- [6] Daiguji H, Oka Y, Shirono K. Nanofluidic diode and bipolar transistor. *Nano Lett* 2005;5(11):2274–80.
- [7] Ramirez P, Garcia-Morales V, Gomez V, Ali M, Nasir S, Ensinger W, Mafe S. Hybrid circuits with nanofluidic diodes and load capacitors. *Phys Rev Appl* 2017;7(6):064035.
- [8] Daiguji H, Yang PD, Szeri AJ, Majumdar A. Electrochemomechanical energy conversion in nanofluidic channels. *Nano Lett* 2004;4(12):2315–21.
- [9] Wang M, Kang Q. Electrochemomechanical energy conversion efficiency in silica nanochannels. *Microfluid Nanofluid* 2010;9(2-3):181–90.
- [10] van der Heyden FHJ, Bonthuis DJ, Stein D, Meyer C, Dekker C. Electrokinetic energy conversion efficiency in nanofluidic channels. *Nano Lett* 2006;6(10):2232–7.
- [11] Hwang J, Sekimoto T, Hsu W-L, Kataoka S, Endo A, Daiguji H. Thermal dependence of nanofluidic energy conversion by reverse electro dialysis. *Nanoscale* 2017;9(33):12068–76.
- [12] Kim SJ, Ko SH, Kang KH, Han J. Direct seawater desalination by ion concentration polarization. *Nat Nanotechnol* 2010;5(4):297–301.
- [13] Lameh S, Ding L, Stein D. Controlled amplification of DNA Brownian motion using electrokinetic noise. *Phys Rev Appl* 2020;14(5):054042.
- [14] Taghipoor M, Bertsch A, Renaud P. Temperature sensitivity of nanochannel electrical conductance. *ACS Nano* 2015;9(4):4563–71.
- [15] Taghipoor M, Bertsch A, Renaud P. Thermal control of ionic transport and fluid flow in nanofluidic channels. *Nanoscale* 2015;7(44):18799–804.
- [16] Wei C, Bard AJ, Feldberg SW. Current rectification at quartz nanopipet electrodes. *Anal Chem* 1997;69(22):4627–33.
- [17] Apel PY, Korchev YE, Siwy Z, Spohr R, Yoshida M. Diode-like single-ion track membrane prepared by electro-stopping. *Nuclear Instruments and Methods in Physics Research Section B: beam interactions with Mater Atoms* 2001;184(3):337–46.
- [18] Siwy Z, Mercik S, Weron K, Spohr R, Wolf A, Grzywna Z. Comparison of single channel potassium current in biological and synthetic systems - dependence on voltage. *Acta Phys Pol B* 2000;31(5):1125–41.
- [19] Siwy Z, Fulinski A. Fabrication of a synthetic nanopore ion pump. *Phys Rev Lett* 2002;89(19):4.
- [20] Siwy Z, Apel P, Dobrev D, Neumann R, Spohr R, Trautmann C, Voss K. Ion transport through asymmetric nanopores prepared by ion track etching. *Nuclear*

- Instruments and Methods in Physics Research Section B: Beam Interactions with Mater Atoms 2003;208(Supplement C):143–8.
- [21] Siwy Z, Apel P, Baur D, Dobrev DD, Korchev YE, Neumann R, Spohr R, Trautmann C, Voss K-O. Preparation of synthetic nanopores with transport properties analogous to biological channels. *Surf Sci* 2003;532(Supplement C): 1061–6.
- [22] Cheng LJ, Guo LJ. Rectified ion transport through concentration gradient in homogeneous silica nanochannels. *Nano Lett* 2007;7(10):3165–71.
- [23] Karnik R, Duan C, Castelino K, Daiguji H, Majumdar A. Rectification of ionic current in a nanofluidic diode. *Nano Lett* 2007;7(3):547–51.
- [24] Vlasiouk I, Siwy ZS. Nanofluidic diode. *Nano Lett* 2007;7(3):552–6.
- [25] Cheng LJ, Guo LJ. Nanofluidic diodes. *Chem Soc Rev* 2010;39(3):923–38.
- [26] Cheng L-J, Guo L-J. Ionic current rectification, breakdown, and switching in heterogeneous oxide nanofluidic devices. *ACS Nano* 2009;3(3):575–84.
- [27] Li J, Li D. A surface charge governed nanofluidic diode based on a single polydimethylsiloxane (PDMS) nanochannel. *J Colloid Interface Sci* 2021;596: 54–63.
- [28] Alizadeh A, Warkiani ME, Wang M. Manipulating electrokinetic conductance of nanofluidic channel by varying inlet pH of solution. *Microfluid Nanofluid* 2017;21 (3):52.
- [29] Alcaraz A, Ramirez P, Garcia-Gimenez E, Lopez ML, Andrio A, Aguilera VM. A pH-tunable nanofluidic diode: electrochemical rectification in a reconstituted single ion channel. *J Phys Chem B* 2006;110(42):21205–9.
- [30] Guo W, Tian Y, Jiang L. Asymmetric ion transport through ion-channel-mimetic solid-state nanopores. *Acc Chem Res* 2013;46(12):2834–46.
- [31] Zhang Z, Kong X-Y, Xiao K, Liu Q, Xie G, Li P, Ma J, Tian Y, Wen L, Jiang L. Engineered asymmetric heterogeneous membrane: a concentration-gradient-driven energy harvesting device. *J Am Chem Soc* 2015;137(46):14765–72.
- [32] Alizadeh A, Zhang L, Wang M. Mixing enhancement of low-Reynolds electroosmotic flows in microchannels with temperature-patterned walls. *J Colloid Interface Sci* 2014;431:50–63.
- [33] Venditti R, Xuan X, Li D. Experimental characterization of the temperature dependence of zeta potential and its effect on electroosmotic flow velocity in microchannels. *Microfluid Nanofluid* 2006;2(6):493–9.
- [34] Revil A, Pezard PA, Glover PWJ. Streaming potential in porous media 1. Theory of the zeta potential. *J Geophys Res* 1999;104(B9):20021–31.
- [35] Peng P-H, Yang H-CO, Tsai P-C, Yeh L-H. Thermal dependence of the mesoscale ionic diode: modeling and experimental verification. *ACS Appl Mater Interfaces* 2020;12(14):17139–46.
- [36] Hsu J-P, Chen Y-C, Chen Y-M, Tseng S. Influence of temperature and electroosmotic flow on the rectification behavior of conical nanochannels. *J Taiwan Inst Chem Eng* 2018;93:142–9.
- [37] Perera RT, Johnson RP, Edwards MA, White HS. Effect of the electric double layer on the activation energy of ion transport in conical nanopores. *J Phys Chem C* 2015;119(43):24299–306.
- [38] Benneker AM, Wendt HD, Lammertink RGH, Wood JA. Influence of temperature gradients on charge transport in asymmetric nanochannels. *PCCP* 2017;19(41): 28232–8.
- [39] Alizadeh A, Wang M. Temperature effects on electrical double layer at solid-aqueous solution interface. *Electrophoresis* 2020;41(12):1067–72.
- [40] Tasaka M, Mizuta T, Sekiguchi O. Mass transfer through polymer membranes due to a temperature gradient. *J Membr Sci* 1990;54(1):191–204.
- [41] Wood JA, Benneker AM, Lammertink RGH. Temperature effects on the electrohydrodynamic and electrokinetic behaviour of ion-selective nanochannels. *J Phys* 2016;28(11):114002.
- [42] Alizadeh A, Wang M. Flexibility of inactive electrokinetic layer at charged solid-liquid interface in response to bulk ion concentration. *J Colloid Interface Sci* 2019; 534:195–204.
- [43] Tasaka M, Abe S, Sugiura S, Nagasawa M. Thermoosmosis through charged membranes. *Biophys Chem* 1977;6(3):271–8.
- [44] Kim K, Kwak HS, Song T-H. A numerical model for simulating electroosmotic micro- and nanochannel flows under non-Boltzmann equilibrium. *FIDyR* 2011;43 (4):041401.
- [45] Alizadeh A, Wang JK, Pooyan S, Mirbozorgi SA, Wang M. Numerical study of active control of mixing in electro-osmotic flows by temperature difference using lattice Boltzmann methods. *J Colloid Interface Sci* 2013;407:546–55.
- [46] Alizadeh A, Wang M. Reverse electro dialysis through nanochannels with inhomogeneously charged surfaces and overlapped electric double layers. *J Colloid Interface Sci* 2018;529:214–23.
- [47] Wang M, Kang Q. Modeling electrokinetic flows in microchannels using coupled lattice Boltzmann methods. *J Comput Phys* 2010;229(3):728–44.
- [48] Yoshida H, Kinjo T, Washizu H. Coupled lattice Boltzmann method for simulating electrokinetic flows: a localized scheme for the Nernst-Planck model. *Commun Nonlinear Sci Numer Simul* 2014;19(10):3570–90.
- [49] Alizadeh A, Wang M. Direct simulation of electroosmosis around a spherical particle with inhomogeneously acquired surface charge. *Electrophoresis* 2017;38 (5):580–95.
- [50] Kitamura A, Fujiwara K, Yamamoto T, Nishikawa S, Moriyama H. Analysis of adsorption behavior of cations onto quartz surface by electrical double-layer model. *J Nucl Sci Technol* 1999;36(12):1167–75.
- [51] Crespy A, Boleve A, Revil A. Influence of the Dukhin and Reynolds numbers on the apparent zeta potential of granular porous media. *J Colloid Interface Sci* 2007;305 (1):188–94.
- [52] Gaudin AM, Fuerstenau DW. Quartz flotation with anionic collectors. *Trans Am Inst Mining Metall Eng* 1955;202(1):66–72.
- [53] Masliyah JH, Bhattacharjee S. *Electrokinetic and colloid transport phenomena*. New Jersey: John Wiley & Sons; 2006.
- [54] Alizadeh A, Hsu W-L, Wang M, Daiguji H. Electroosmotic flow: From microfluidics to nanofluidics. *Electrophoresis* 2021;42(7-8):834–68.
- [55] Overbeek JTC. *Colloid science, 1. Irreversible Systems*; 1952.